MODELING THE PASSIVE MICROWAVE REMOTE SENSING OF SNOW USING DENSE MEDIA RADIATIVE TRANSFER THEORY WITH NMM3D ROUGH-SURFACE BOUNDARY CONDITIONS

Zhongxin Li,[1] Yunhua Tan,[1] and Leung Tsang[1,2]
[1] Wireless Communications Research Center
City University of Hong Kong
Hong Kong SAR
[2] Electrical Engineering Department
University of Washington
Box 352500
Seattle, WA 98195-2500

ABSTRACT: *The effects of volume scattering and rough-surface scattering in passive microwave remote sensing are treated. The volume-scattering model is based on dense medium radiative transfer (DMRT) theory with quasicrystalline approximation (QCA) for densely distributed sticky particles. The rough-surface bistatic scattering and emission are modeled using the numerical Maxwell model of 3D simulations (NMM3D). The bistatic scattering coefficients and emissivity of rough surfaces are utilized as the boundary conditions for the DMRT. Full multiple scattering solutions are calculated by solving the DMRT numerically. The results are illustrated for a layer of dry snow over rough ground at 18.7 and 36.5 GHz.* © 2006 Wiley Periodicals, Inc.
Microwave Opt Technol Lett 48: 557–562, 2006; Published online in Wiley InterScience (www.interscience.wiley.com). DOI 10.1002/mop.21407

1. INTRODUCTION

In microwave remote sensing of snow, there are volume scattering from the ice grains and rough-surface scattering of the interface between the snow and the ground. In the past, the combined volume scattering and surface scattering was treated using classical radiative transfer theory and rough-surface boundary conditions based on physical optics or the small-perturbation method [1, 2]. In this paper, the two effects are studied by using the dense media radiative transfer theory (DMRT) with rough-surface boundary conditions of the numerical Maxwell model of 3D simulations (NMM3D) [3]. For the radiative transfer part, the DMRT theory is based on the quasicrystalline approximation (QCA) for sticky particles that can be of moderate size compared with wavelength. The DMRT theory includes the effects of correlated scattering and coherent field interaction in the near- and intermediate-field ranges [4]. In the past, the rough-surface effects have been modeled using analytic methods such as Kirchhoff approximation or small perturbation [1, 2]. However, with the advances of computers and computation methods, we can calculate the rough-surface effects through numerical solutions of 3D Maxwell equations. The NMM3D simulations are based on the sparse matrix canonical-grid method (SMCG), which is a fast method of solving the matrix equation, associated with the surface-integral equation [3]. Gaussian random rough surfaces with exponential correlation functions are used because they are more applicable to land surfaces than Gaussian correlation function [5]. Rao–Wilton–Glisson (RWG) basis functions are used in NMM3D to improve the accuracy of the solution, particularly in relation to energy conservation [5].
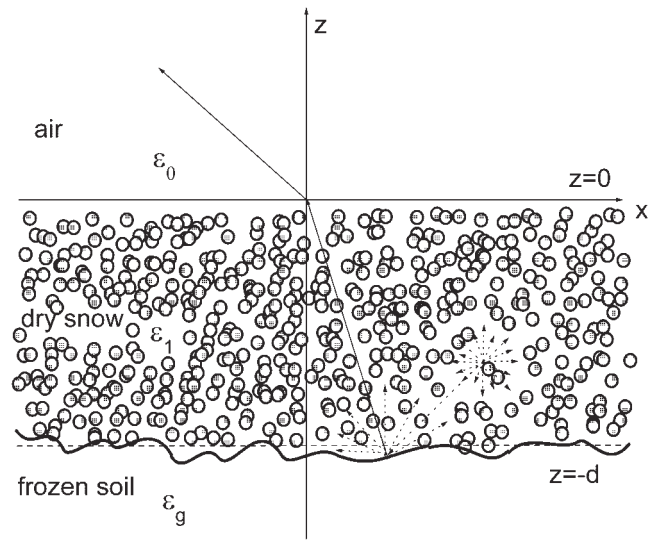

Figure 1 Geometry of the problem for simulations using the DMRT model

In section 2, the DMRT theory is described. The bistatic coefficients of rough-surface scattering obtained by NMM3D are incorporated in rough-surface boundary conditions for DMRT in passive microwave remote sensing. In section 3, results for passive microwave remote sensing at 18.7 and 36.5 GHz of a layer of dry snow overlaying rough ground are illustrated. In order to rigorously study the frequency dependence of microwave signatures, we use the same set of physical parameters of grain sizes, fractional volumes, and rough-surface rms height and correlation lengths for both 18.7 and 36.5 GHz to calculate the brightness temperatures.

2. METHODOLOGY

2.1. DMRT Model for Volume Scattering

The sticky particle model is used in this DMRT model. In the sticky particle model, the snow grains are allowed to stick together to form clusters. A distinguishing feature of the dense media model is that although the particles are small compared with wavelength, the frequency dependence of volume scattering is weaker than the classical Rayleigh prediction of frequency to the fourth power. This is because of the aggregate nature of the sticky particles. Secondly, the mean cosine of the scattering is not equal to zero, as in the classical Rayleigh phase matrix. The pair distribution functions of sticky particles are used [4, 6].

Consider a layer of snow overlaying ground with a rough surface. The dry snow cover is modeled by a layer of densely-distributed sticky spherical ice particles embedded in air with permittivity ε_0 (Fig. 1). The effective permittivity in snow for the coherent wave is ε_1. The layer thickness is d. The soil has a permittivity $\varepsilon_g = \varepsilon_g' + i\varepsilon_g''$. The DMRT equations for passive remote sensing are in the following form [2]:

$$
\cos\theta \frac{d\bar{I}_u(z, \theta)}{dz} = -\kappa_e \bar{I}_u(z, \theta) + \int_0^{\pi/2} d\theta' \sin\theta' \cdot \bar{\bar{P}}(\theta; \theta') \cdot \bar{I}_u(z, \theta')
$$

$$
+ \int_0^{\pi/2} d\theta' \sin\theta' \cdot \bar{\bar{P}}(\theta; \pi - \theta') \cdot \bar{I}_d(z, \theta') + \kappa_a \cdot \bar{T}, \quad (1)
$$

$$-\cos\theta\frac{d\bar{I}_d(z,\theta)}{dz} = -\kappa_e\bar{I}_d(z,\theta) + \int_0^{\pi/2} d\theta'\sin\theta'\cdot\bar{\bar{P}}(\pi$$

$$-\theta;\theta')\cdot\bar{I}_u(z,\theta') + \int_0^{\pi/2} d\theta'\sin\theta'\cdot\bar{\bar{P}}(\pi-\theta;\pi-\theta')\cdot\bar{I}_d(z,\theta')$$

$$+\kappa_a\cdot\bar{T}, \quad (2)$$

where $\bar{I}_u(z,\theta)$ and $\bar{I}_d(z,\theta)$ are 2×1 vectors, given by

$$\bar{I}_u(z,\theta) = \begin{bmatrix} I_u^v(z,\theta) \\ I_u^h(z,\theta) \end{bmatrix}, \quad (3)$$

$$\bar{I}_d(z,\theta) = \begin{bmatrix} I_d^v(z,\theta) \\ I_d^h(z,\theta) \end{bmatrix}, \quad (4)$$

and $\bar{\bar{P}}$ is a 2×2 phase matrix with

$$\bar{\bar{P}}(\theta,\theta') = \begin{bmatrix} p_{vv}(\theta,\theta') & p_{vh}(\theta,\theta') \\ p_{hv}(\theta,\theta') & p_{hh}(\theta,\theta') \end{bmatrix}, \quad (5)$$

and $\bar{T}$ is a 2×1 vector:

$$\bar{T} = \begin{bmatrix} T \\ T \end{bmatrix}. \quad (6)$$

In Eqs. (1)–(6), T is the physical temperature of snow, v and h denote vertical and horizontal polarization, respectively, and κ_e, κ_a are snow's extinction rate and absorbing coefficient, respectively [4, 7]. Using QCA theory, we calculate the effective propagation constant of snow, which depends on the ice grain's fractional volume f, diameter $2a$, and permittivity ε_p. Using f, $2a$, and ε_p, the effective permittivity ε_1 of snow is calculated from the square of the ratio of the effective propagation constant of snow to the propagation constant of air.

For the surface between snow and air ($z = 0$), the boundary condition is

$$\bar{I}_d(\theta, z=0) = \bar{\bar{r}}_{10}(\theta)\bar{I}_u(\theta, z=0), \quad (7)$$

where

$$\bar{\bar{r}}_{10}(\theta) = \begin{bmatrix} r_{10}^v(\theta) & 0 \\ 0 & r_{10}^h(\theta) \end{bmatrix}$$

is the flat surface's reflectivity.

For the rough surface of soil ($z = -d$), the boundary condition is

$$\bar{I}_u(\theta, z=-d)\cdot\cos\theta = \bar{\bar{\gamma}}_c(\theta)\cdot\bar{I}_d(\theta, z=-d)\cdot\cos\theta$$

$$+\int_0^{\pi/2} d\theta'\sin\theta'\cdot\int_0^{2\pi} d\varphi'\bar{\bar{\gamma}}_{ic}(\theta,\varphi;\theta',\varphi')\cdot\cos\theta\cdot\bar{I}_d(\theta,z=-d)$$

$$+\bar{e}(\theta)T_g\cos\theta, \quad (8)$$

where

$$\bar{\bar{\gamma}}_c(\theta) = \begin{bmatrix} \gamma_c^{vv}(\theta) & 0 \\ 0 & \gamma_c^{hh}(\theta) \end{bmatrix}$$

and

$$\bar{\bar{\gamma}}_{ic}(\theta,\varphi;\theta',\varphi') = \begin{bmatrix} \gamma_{ic}^{vv}(\theta,\varphi;\theta',\varphi') & \gamma_{ic}^{vh}(\theta,\varphi;\theta',\varphi') \\ \gamma_{ic}^{hv}(\theta,\varphi;\theta',\varphi') & \gamma_{ic}^{hh}(\theta,\varphi;\theta',\varphi') \end{bmatrix}$$

are the coherent and incoherent bistatic scattering coefficients of rough surfaces, respectively. In Eq. (8),

$$\bar{e}(\theta) = \begin{bmatrix} e^{vv}(\theta) & 0 \\ 0 & e^{hh}(\theta) \end{bmatrix}$$

is the microwave thermal emissivity of the rough soil surface and T_g is the soil's brightness temperature.

We set

$$\bar{\bar{\Gamma}}_{ic}(\theta,\theta') = \int_0^{2\pi} d\varphi'\bar{\bar{\gamma}}_{ic}(\theta,\varphi;\theta',\varphi'), \quad (9)$$

and then we obtain

$$\cos\theta\cdot\bar{I}_u(\theta, z=-d) = \cos\theta\cdot\bar{\bar{\gamma}}_c(\theta)\cdot\bar{I}_d(\theta, z=-d)$$

$$+\int_0^{\pi/2} d\theta'\sin\theta'\cdot\bar{\bar{\Gamma}}_{ic}(\theta,\theta')\cos\theta'\cdot\bar{I}_d(\theta,z=-d) + \bar{e}(\theta)T_g\cos\theta.$$

$$(10)$$

After solving the DMRT equations and imposing the boundary conditions, the brightness temperature is calculated by

$$\bar{T}_B(\theta_0) = [\bar{\bar{I}} - \bar{\bar{r}}_{10}(\theta)]\bar{I}_u(\theta, z=0), \quad (11)$$

where

$$\theta_0 = \sin^{-1}\left(\frac{\sin\theta}{\sqrt{\varepsilon_1}}\right)$$

is the observation angle in the air region of the Snell's law, and

$$\bar{T}_B(\theta_0) = [T_B^v(\theta_0) \quad T_B^h(\theta_0)]^T.$$

Applying discrete ordinate-eigenanalysis method to the DMRT equations, the directions are discretized into N directions upward and N directions downward.

We set $\mu = \cos\theta$. Then μ_i with $i = 1, 2, \ldots, N$ denotes the positions of the zeros of the Legendre polynomial $P_{2N}(\mu)$. α_i with $i = 1, 2, \ldots, N$, denotes the corresponding Christoffel weights.

After discretization of angles θ, $\bar{\bar{\mu}}$ is a $2N \times 2N$ diagonal matrix:

$$\bar{\bar{\mu}} = \begin{bmatrix} \mu_1 & & & & & \\ & \ddots & & & & \\ & & \mu_N & & & \\ & & & \mu_i & & \\ & & & & \ddots & \\ & & & & & \mu_N \end{bmatrix}, \quad (12)$$

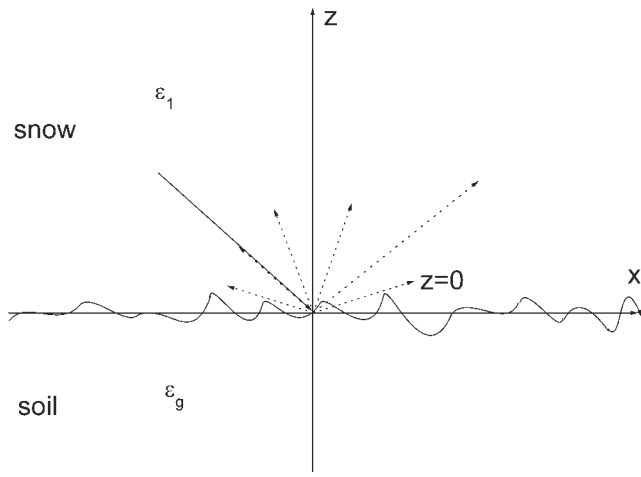$\bar{\bar{\alpha}}$ is a $2N \times 2N$ diagonal matrix:

Figure 2 Geometry of the problem for simulations using NMM3D

$$
\bar{\bar{\alpha}} = \begin{bmatrix} \alpha_1 & & & & & \\ & \ddots & & & & \\ & & \alpha_N & & & \\ & & & \alpha_i & & \\ & & & & \ddots & \\ & & & & & \alpha_{N} \end{bmatrix}, \tag{13}
$$

and $\bar{\bar{e}}$ is a $2N \times 2N$ matrix:

$$
\bar{\bar{e}} = \begin{bmatrix} \bar{\bar{e}}^{vv} & 0 \\ 0 & \bar{\bar{e}}^{hh} \end{bmatrix}, \tag{14}
$$

where $\bar{\bar{e}}^{vv}$ and $\bar{\bar{e}}^{hh}$ are $N \times N$ diagonal matrices:

$$
\bar{\bar{e}}^{vv/hh} = \begin{bmatrix} e^{vv/hh}(\mu_1) & & & & \\ & \ddots & & & \\ & & e^{vv/hh}(\mu_i) & & \\ & & & \ddots & \\ & & & & e^{vv/hh}(\mu_N) \end{bmatrix}. \tag{15}
$$

$\bar{\bar{\gamma}}_c$ is a $2N \times 2N$ matrix:

$$
\bar{\bar{\gamma}}_c = \begin{bmatrix} \bar{\bar{\gamma}}_c^{vv} & 0 \\ 0 & \bar{\bar{\gamma}}_c^{hh} \end{bmatrix}, \tag{16}
$$

where $\bar{\bar{\gamma}}_c^{vv}$ and $\bar{\bar{\gamma}}_c^{hh}$ are $N \times N$ diagonal matrices:

$$
\bar{\bar{\gamma}}_c^{vv/hh} = \begin{bmatrix} \gamma_c^{vv/hh}(\mu_1) & & & & \\ & \ddots & & & \\ & & \gamma_c^{vv/hh}(\mu_i) & & \\ & & & \ddots & \\ & & & & \gamma_c^{vv/hh}(\mu_N) \end{bmatrix}. \tag{17}
$$

$\bar{\bar{\Gamma}}_{ic}$ is a $2N \times 2N$ matrix:

$$
\bar{\bar{\Gamma}}_{ic} = \begin{bmatrix} \bar{\bar{\Gamma}}_{ic}^{vv} & \bar{\bar{\Gamma}}_{ic}^{vh} \\ \bar{\bar{\Gamma}}_{ic}^{hv} & \bar{\bar{\Gamma}}_{ic}^{hh} \end{bmatrix}, \tag{18}
$$

where $\bar{\bar{\Gamma}}_{ic}^{vv}$, $\bar{\bar{\Gamma}}_{ic}^{vh}$, $\bar{\bar{\Gamma}}_{ic}^{hv}$, and $\bar{\bar{\Gamma}}_{ic}^{hh}$ are $N \times N$ matrices, respectively, for example:

$$
\bar{\bar{\Gamma}}_{ic}^{vv} = \begin{bmatrix} \Gamma_{ic}^{vv}(\mu_1, \mu_1) & \cdots & \Gamma_{ic}^{vv}(\mu_1, \mu_i) & \cdots & \Gamma_{ic}^{vv}(\mu_1, \mu_N) \\ \vdots & \ddots & \vdots & \ddots & \vdots \\ \Gamma_{ic}^{vv}(\mu_i, \mu_1) & \cdots & \Gamma_{ic}^{vv}(\mu_i, \mu_i) & \cdots & \Gamma_{ic}^{vv}(\mu_i, \mu_N) \\ \vdots & \ddots & \vdots & \ddots & \vdots \\ \Gamma_{ic}^{vv}(\mu_N, \mu_1) & \cdots & \Gamma_{ic}^{vv}(\mu_N, \mu_i) & \cdots & \Gamma_{ic}^{vv}(\mu_N, \mu_N) \end{bmatrix}. \tag{19}
$$

$\bar{I}_u$ and $\bar{I}_d$ are $2N \times 1$ vectors:

$$
\bar{I}_{u/d} = [I_{u/d}^v(\mu_1) \quad \cdots \quad I_{u/d}^v(\mu_N) \quad I_{u/d}^h(\mu_1) \quad \cdots \quad I_{u/d}^h(\mu_N)]^T. \tag{20}
$$

The rough-surface scattering boundary-condition equation can then be approximated by a quadrature formula as follows:

$$
\bar{I}_u\,(z = -d) = (\bar{\bar{\gamma}}_c + \bar{\bar{\mu}}^{-1} \cdot \bar{\bar{\Gamma}}_{ic} \cdot \ddot{\alpha} \cdot \bar{\bar{\mu}}) \cdot \bar{I}_d\,(z = -d) + \bar{\bar{e}} \cdot T_g. \tag{21}
$$

We set

$$
\bar{\bar{\gamma}}_g = (\bar{\bar{\gamma}}_c + \bar{\bar{\mu}}^{-1} \cdot \bar{\bar{\Gamma}}_{ic} \cdot \bar{\bar{\alpha}} \cdot \bar{\bar{\mu}}), \tag{22}
$$

and then we obtain

$$
\bar{I}_u\,(z = -d) = \bar{\bar{\gamma}}_g \bar{I}_d\,(z = -d) + \bar{\bar{e}} \cdot T_g. \tag{23}
$$

2.2. Numerical Implementation of Rough-Surface Boundary Conditions

Consider a wave impinging from snow onto the ground. The ground–snow interface has a random height profile (Fig. 2). The incident electromagnetic wave is tapered so that the illuminated rough surface can be plane-confined to a finite size [3, 5]. Numerical simulations of Maxwell equations are performed using the NMM3D, in which the PMCHW formulation with RWG basis functions are used [3, 5]. We use the SMCG fast matrix solver.

Using NMM3D, we calculate the bistatic scattering coefficients normalized by the incident power. The bistatic scattering coefficients are [3]
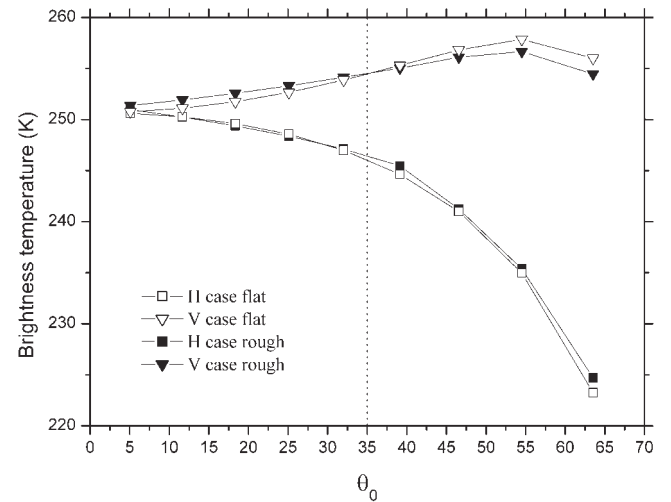

Figure 3 Comparison between rough and flat surfaces at different observation angles ($f = 18.7$ GHz, $2a = 0.2$ mm)
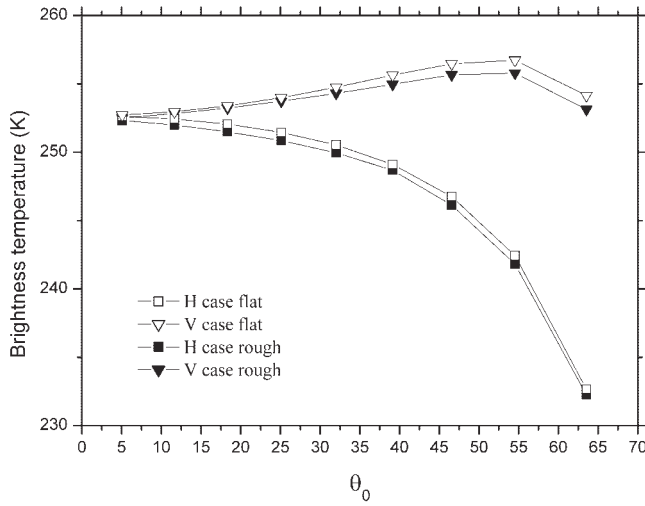
Figure 4 Comparison of dry snow on rough and flat surfaces of frozen soil at different observation angles ($f = 36.5$ GHz, $2a = 0.2$ mm)

$$\gamma_{\alpha\beta}(\theta_s, \varphi_s; \theta_i, \varphi_i) = \frac{\langle |\bar{E}_\alpha^s|^2 \rangle}{2\eta_1 P_\beta^{inc}}, \quad (24)$$

where β is the incident-wave polarization and α is the scattered-wave polarization. The angular brackets $\langle$ and $\rangle$ denote taking averages over realizations.

For surfaces of infinite extent, the coherent wave is a delta function in the specular direction. In numerical simulations, because the surface is of finite size, the coherent wave is of finite angular width. In the simulations, the coherent bistatic scattering coefficients from the finite surface are calculated by

$$\gamma_{\alpha\beta}^c(\theta_s, \varphi_s; \theta_i, \varphi_i) = \frac{|\langle \bar{E}_\alpha^s \rangle|^2}{2\eta_1 P_\beta^{inc}}. \quad (25)$$

Incoherent bistatic coefficients are calculated by the subtraction of the coherent scattering from the total scattering as follows:
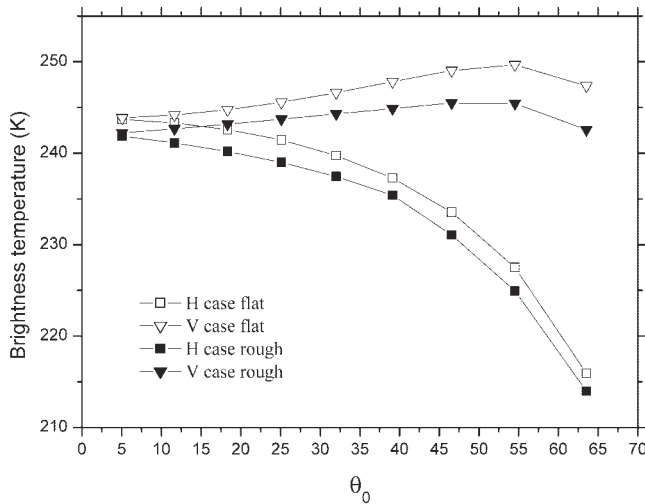

Figure 5 Comparison of dry snow on rough and flat surfaces of frozen soil at different observation angles ($f = 18.7$ GHz, $2a = 0.6$ mm)
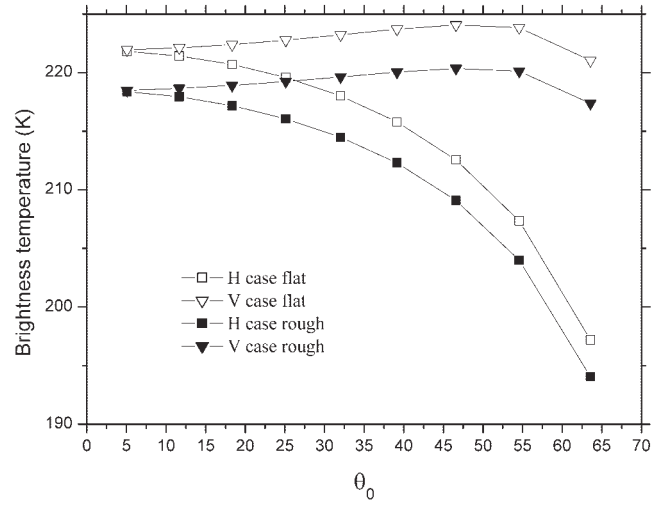

Figure 6 Comparison of dry snow on rough and flat surfaces of frozen soil at different observation angles ($f = 36.5$ GHz, $2a = 0.6$ mm)

$$\gamma_{\alpha\beta}^{ic}(\theta_s, \varphi_s; \theta_i, \varphi_i) = \gamma_{\alpha\beta}(\theta_s, \varphi_s; \theta_i, \varphi_i) - \gamma_{\alpha\beta}^c(\theta_s, \varphi_s; \theta_i, \varphi_i). \quad (26)$$

To obtain the coherent reflectivity for surface of infinite extent, we integrate the coherent bistatic scattering coefficients of finite surfaces over scattered angles. The coherent reflectivity at incident angle (θ_i, φ_i) is

$$\gamma_c(\theta_i, \varphi_i) = \int_0^{\pi/2} \sin \theta_s d\theta_s \int_0^{2\pi} d\varphi_s \gamma_{\alpha\beta}^c(\theta_s, \varphi_s; \theta_i, \varphi_i). \quad (27)$$

Emissivity of the rough surface at incident angle (θ_i, φ_i) is transmissivity, which by reciprocity and energy conservation is equal to

$$e_\alpha(\theta_i, \varphi_i) = 1 - \int_0^{\pi/2} \sin \theta_s d\theta_s \int_0^{2\pi} d\varphi_s [\gamma_{h\alpha}(\theta_s, \varphi_s; \theta_i, \varphi_i)$$
$$+ \gamma_{v\alpha}(\theta_s, \varphi_s; \theta_i, \varphi_i)]. \quad (28)$$
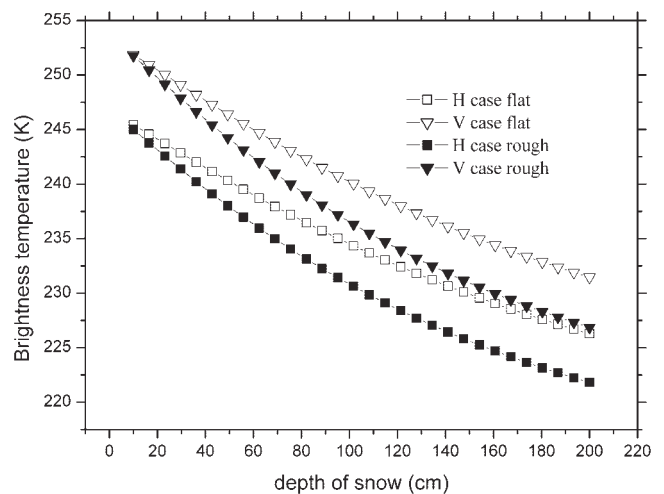

Figure 7 Comparison of dry snow on rough and flat surfaces of frozen soil at different dry snow depths ($f = 18.7$ GHz, $\theta_0 = 30°$)
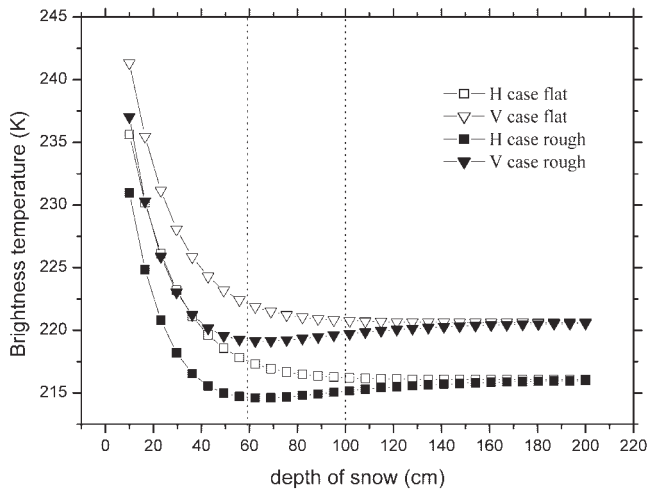
Figure 8 Comparison of dry snow on rough and flat surfaces of frozen soil at different dry snow depths ($f = 36.5$ GHz, $\theta_0 = 30°$)

When the applying discrete ordinate-eigenanalysis method to the DMRT Eqs. (1) and (2) and rough-surface boundary condition Eq. (10), N μ_i values and N α_i values will be used. Generally, the choice of the order of quadrature N depends on the angular variation of the integrand. We have used $N = 16$ in the simulations. There are 16 incident angles in θ'. Assuming azimuthal symmetry, we can take φ' to be equal to 0. To obtain $\bar{\bar{\Gamma}}_{ic}(\theta, \theta')$ for 16 θ and 16 θ', we calculate, for each θ', $\gamma_{\alpha\beta}^{ic}$ $(\theta, \phi; \theta', \phi' = 0)$ for 16 θ and many φ. Then we use integration over φ to obtain $\bar{\bar{\Gamma}}_{ic}(\theta, \theta')$, as indicated in Eq. (9). The surface area needs to increase when the incident angle increases [5]. In the simulations, we use a surface area of 8×8 wavelengths. The surface is not large enough when the incident angle exceeds 60°. We know that when the incident angle is large, the forward scattering in the specular direction will be dominant and will resemble that of flat surface. Thus for an incident angle larger than 60°, we use the flat-surface results for the boundary conditions of the radiative transfer equation.

3. NUMERICAL RESULTS AND DISCUSSIONS

We illustrate the brightness temperatures. The dry snow and frozen soil temperatures are all 260°K. The frequencies are 18.7 and 36.5
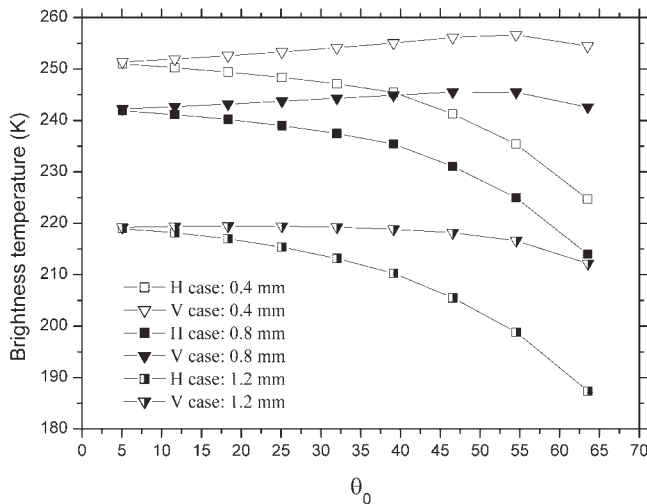

Figure 9 Brightness temperatures: varying grain size and as a function of angle ($f = 18.7$ GHz)
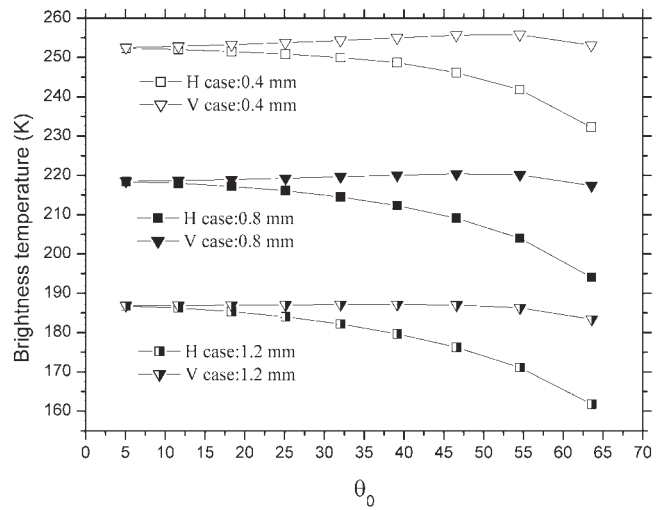

Figure 10 Brightness temperatures: varying grain size and as a function of angle ($f = 36.5$ GHz)

GHz. The rough-surface parameters have rms height of 0.4 mm and correlation length 2.8 mm. The frozen soil's permittivity is $\varepsilon_g = 2.86 + i0.24$. The permittivities of ice grains are $\varepsilon_p = 3.15 + i0.002$ at 18.7 GHz and $\varepsilon_p = 3.15 + i0.0039$ at 36.5 GHz. Unless stated otherwise, the fractional volume is 30%, the snow layer thickness is 50 cm, and the observation angle is 30°. The stickiness parameter is $\tau = 0.1$.

3.1. Comparison of Brightness Temperatures Between Rough and Flat Surfaces for the Small-Grain-Size Case

In Figures 3–6 we compare the brightness temperatures between rough surfaces and flat surfaces. To show the roughness effects, we firstly choose grain diameter equal to 0.2 mm in Figures 3 and 4 so that the volume-scattering effects are small.

Figure 3 shows the brightness temperatures at 18.7 GHz as a function of angles θ_0 in the air region. For horizontal polarization, the brightness temperature for the rough surface is larger than that of flat surface. For vertical polarization, when the observation angle is less than 35°, the brightness temperature of the rough surface is larger than that of the flat surface. When the observation angle is larger than 35°, the brightness temperature for the rough
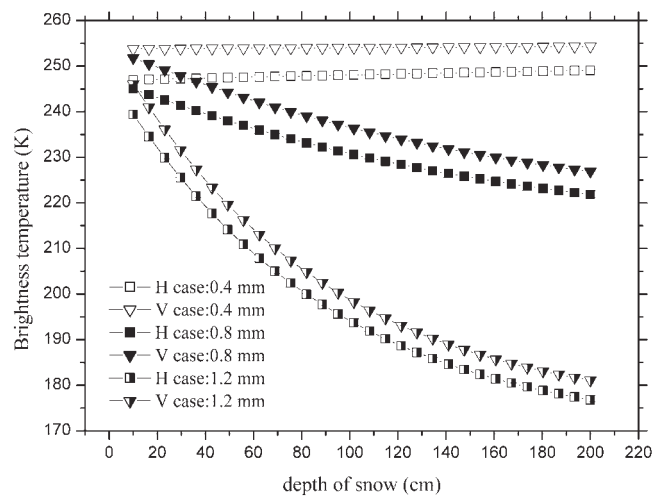

Figure 11 Brightness temperatures: varying grain size and as a function of snow depth ($f = 18.7$ GHz)
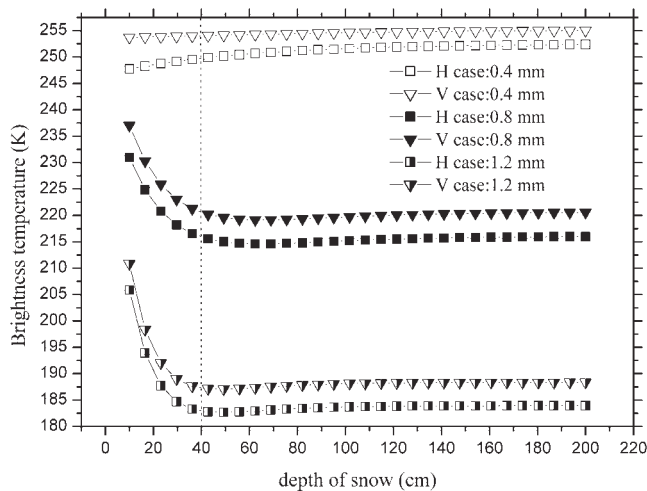
Figure 12 Brightness temperatures: varying grain size and as a function of snow depth ($f = 36.5$ GHz)

REFERENCES

1. C.M. Lam and A. Ishimaru, Mueller matrix calculation for a slab of random medium with both random rough surfaces and discrete particles, IEEE Trans Antennas Propagat 42 (1994), 145–156.
2. L. Zhou, L. Tsang, and D. Chen, Polarimetric microwave remote sensing of wind vectors with foam covered rough ocean surfaces, Radio Sci 38 (2003).
3. L. Tsang, J.A. Kong, K.H. Ding, and C.O. Ao, Scattering of electromagnetic waves vol. 2: Numerical simulations, Wiley–Interscience, New York, 2001.
4. L. Tsang and J.A. Kong, Scattering of electromagnetics waves vol. 3: Advanced topics, Wiley–Interscience, New York, 2001.
5. L. Zhou, L. Tsang, V. Jandhyala, Q. Li, and C.H. Chan, Emissivity simulations in passive microwave remote sensing with 3D numerical solutions of Maxwell equations, IEEE Trans Geosci and Remote Sensing 42 (2004), 1739–1748.
6. K.H. Ding, L.M. Zurk, and L. Tsang, Pair distribution functions and attenuation rates for sticky particles in dense media, J Electromagn Waves Applic 8 (1994), 1585–1604.
7. L. Tsang, J.A. Kong, and K.H. Ding, Scattering of electromagnetics waves vol. 1: Theories and applications, Wiley–Interscience, New York, 2000.

© 2006 Wiley Periodicals, Inc.

surface is smaller than that of the flat surface. That is because the Brewster angle between ground and snow is 50°. The 50° angle in snow corresponds to 35° in air by Snell's law. However, at the higher frequency of 36.5 GHz in Figure 4, volume scattering becomes important and obscures the Brewster-angle effect of the snow–ground interface. At 36.5 GHz, rough-surface brightness temperatures are lower than that of flat surface for both V-polarization and H-polarization.

Figures 5 and 6 compare results of flat and rough surfaces as a function of observation angle for the case of larger grain size of diameter equal to 0.6 mm. Volume scattering becomes important at 18.7 GHz. The Brewster-angle effect of the snow–ground interface disappears. The roughness decreases the brightness temperatures.

Figures 7 and 8 compare the results of flat and rough surfaces as a function of depth of snow; the grain size is also 0.6 mm. At 18.7 GHz, since the observation angle is 30° (which is less than the Brewster angle of 35°), the brightness temperatures of rough surface is smaller than flat surface for V-polarization.

In Figure 8, we see that at 36.5 GHz, saturation occurs at large snow depth. Volume scattering becomes dominant and roughness has a negligible effect.

3.2. Brightness-Temperature Variations with Grain Size and Snow Depth

Figures 9 and 10 show the angular variations of brightness temperatures for several grain-size diameters. The brightness temperatures decrease with increasing grain size. Emission from the ground is scattered and cannot reach the air region, thus accounting for the decrease in brightness temperatures.

Figures 11 and 12 show that, for small grain size, brightness temperatures depend weakly on the thicknesses of the snow layer. For larger grain size, brightness temperatures decrease with snow depth at 18.7 GHz. For 36.5 GHz, saturation effects occur as a function of snow depth.

ACKNOWLEDGMENTS

RECONFIGURABLE AND TUNABLE MICROWAVE-PHOTONICS BANDPASS-SLICING FILTER USING A DYNAMIC GAIN EQUALIZER

Hervé Gouraud,[1] Philippe Di Bin,[1] Laurent Billonnet,[1] Bernard Jarry,[1] Erwan Lecroizier,[2] Michel Barge,[2] and Jean-Louis de Bougrenet De La Tocnaye[3]
[1] IRCOM, UMR CNRS n°6615
123, avenue Albert Thomas
87060 Limoges Cedex, France
[2] OPTOGONE S.A.
305, rue C.E. Shannon
29280 Plouzane, France
[3] Optics Department, UMR CNRS 6032 Foton
ENST-Bretagne, Technopôle Brest–Iroise–CS 83818
29238 BREST Cedex 3, France

ABSTRACT: *We propose an optimized structure of a tunable and reconfigurable microwave-photonics filter. The structure exploits the capability of a high-precision dynamic-gain equalizer (DGE) to modify the optical spectrum of the broadband light source of a slicing filter. Independent tunability and reconfigurability is obtained due to the optimization of the dispersion properties of the optical fiber line. An experimental demonstration is given that illustrates the versatility and efficiency of the setup.* © 2006 Wiley Periodicals, Inc.

1. INTRODUCTION

The optical processing of high-frequency signals has been the matter of an intense research activity for more than ten years. The most frequently developed function is bandpass filtering for telecommunications as well as for radar applications. Numerous photonic structures have been proposed, taking advantage of the